# MCViNE – An object oriented Monte Carlo neutron ray tracing simulation package

Jiao Y. Y. Lin[a,*], Hillary L. Smith[b], Garrett E. Granroth[c], Douglas L. Abernathy[d], Mark D. Lumsden[d], Barry Winn[d], Adam A. Aczel[d], Michael Aivazis[a], Brent Fultz[b]

[a] *Caltech Center for Advanced Computing Research, California Institute of Technology*
[b] *Department of Applied Physics and Materials Science, California Institute of Technology*
[c] *Neutron Data Analysis and Visualization Division, Oak Ridge National Laboratory*
[d] *Quantum Condensed Matter Division, Oak Ridge National Laboratory*

**Abstract**

MCViNE (Monte-Carlo VIrtual Neutron Experiment) is a versatile Monte Carlo (MC) neutron ray-tracing program that provides researchers with tools for performing computer modeling and simulations that mirror real neutron scattering experiments. By adopting modern software engineering practices such as using composite and visitor design patterns for representing and accessing neutron scatterers, and using recursive algorithms for multiple scattering, MCViNE is flexible enough to handle sophisticated neutron scattering problems including, for example, neutron detection by complex detector systems, and single and multiple scattering events in a variety of samples and sample environments. In addition, MCViNE can take advantage of simulation components in linear-chain-based MC ray tracing packages widely used in instrument design and optimization, as well as NumPy-based components that make prototypes useful and easy to develop. These developments have enabled us to carry out detailed simulations of neutron scattering experiments with non-trivial samples in time-of-flight inelastic instruments at the Spallation Neutron Source. Examples of such simulations for powder and single-crystal samples with various scattering kernels, including kernels for phonon and magnon scattering, are presented. With simulations that closely reproduce experimental results, scattering mechanisms can be turned on and off to determine how they contribute to the measured scattering intensities, improving our understanding of the underlying physics.

*Keywords:* neutron scattering, Monte Carlo simulation, ray-tracing, inelastic, spectrometry

*Corresponding author
*Email address:* linjiao@caltech.edu (Jiao Y. Y. Lin )

## 1. Introduction

Data analysis for neutron time-of-flight spectroscopy has predominantly been a conversion of raw data to intensities with instrument independent units; namely $S(\mathbf{Q}, \omega)$. This approach has been the basis for many studies, but it has become clear that in some cases this simple "reduction" will not suffice (see, for example, [1, 2, 3, 4, 5, 6, 7, 8, 9]).

As neutron instruments gain more flux and capabilities, measurements of complex samples have become more common. Traditional analysis procedures make assumptions about how signals from various scattering processes overlap, the convolution of the instrument resolution function with the sample scattering function, and the contribution to scattering from sample environments. With higher count rates, smaller effects become statistically significant, and it is important to develop methods to interpret them.

The overlap of scattering processes, such as nuclear and magnetic scattering, is often treated simply by fitting one component to a function. More accurate assessment of these contributions can provide a greater level of detail in analysis of data. Additionally, the instrument resolution is usually accounted for by a convolution with an analytical or numerical resolution function. The complexity of modern instrument design demands a more complex resolution function taking into account a greater level of detail of instrument characteristics, sample, and detectors. Sample environment capabilities continue to allow new ranges of temperature and pressure to be examined, but complex systems lead to additional scattering contributions that require interpertation.

Full Monte Carlo (MC) simulations of neutron scattering experiments should be able to take into account details such as multiple scattering and instrument resolution naturally, and could reduce the number of specialized analysis software packages needed in data analysis workflows. However, data analysis for complex measurements often requires more sophisticated modeling, sometimes even molecular dynamics and quantum chemistry simulations, which demands a new level of computing resources and expertise. Adopting the additional complexity of MC simulations in data analysis may discourage researchers from taking advantage of this approach. MC simulations have been difficult to set up, and integration of MC simulations within the data analysis workflow is not routine today.

MCS[10] and MSCAT[11] were early packages that used Monte Carlo methods to compute multiple scattering. Later, several general-purpose Monte Carlo neutron instrument simulation packages were developed and optimized to help design neutron instruments, such as McStas [12, 13], VITESS [14], IDEAS [15], and NISP [16]. Less-general-purpose MC programs exist in some popular neutron data analysis software packages, including DISCUS [17, 18, 19] and RESTRAX [20, 21]. In comparison, relatively few studies [22, 23, 24, 25, 26] have employed full-fledged Monte Carlo ray tracing to help elucidate experimental results from neutron scattering interments, while there are growing efforts on performing virtual neutron experiments using MC ray tracing [27, 28, 29, 30, 31]. MCViNE[32] is designed to easily allow complex studies (see [9] for an exam-

ple) and therefore should accelerate the use of Monte Carlo ray tracing in the analysis of experimental data.

The improvements in computing over the last decades include hardware, the emergence of object-oriented languages C++ and Python, and advances in software design [33]. For MC simulations of neutron scattering experiments, the impact of these improvements on modern software engineering practice, especially object-oriented language features, is still being realized. MCViNE [32] was developed in the DANSE project [34], and its goal is to simplify the set-up of Monte Carlo ray tracing simulations of neutron experiments, making it possible for non-experts to run simulations of non-trivial samples and sample assemblies and analyze neutron data with more quantitative accuracy. The treatment of neutron scattering in MCViNE goes beyond the typical approach of simulating a linear sequence of neutron components: MCViNE uses a hierarchical representation of neutron scatterers, and it employs object-oriented programming (OOP) instead of the imperative programing paradigm popular in other software. By taking advantage of OOP design patterns as well as recursive algorithms, the MCViNE architecture supports an easily extensible library for scattering kernels. This approach allows for maximum flexibility, extensibility, and reuse of scatterer arrangements, geometrical shapes, and scattering mechanisms, and hence improves the sustainability of the software.

The software engineering design of the MCViNE framework is described here, including some key abstractions, and algorithms built on top of those abstractions. Section 2 presents an overview of the architecture of the MCViNE software framework, and explains how the software constructs in MCViNE allow full extensibility for scattering mechanisms, especially the hierarchical representation of neutron scatterers. Algorithms for multiple scattering and neutron detection in a detector system are then presented. Examples of MCViNE simulations for powder and single-crystal experiments are presented in Section 3.

## 2. The MCViNE software package

### *2.1. Architecture Overview*

There are two classes of Monte Carlo (MC) neutron ray tracing software packages. The first class takes a linear approach, and is in widespread use because it has proved critical for instrument design (see, for example, [35, 36, 37, 38, 39, 40, 41, 42, 43, 44] ). It includes packages such as McStas[12, 13], Vitess[14], and Ideas[15]. The second class has inherent support for multiple scattering including MCS[10], MSCAT[11], and NISP[16]. For example, MSCAT is not implemented using the linear execution structure, and handles multiple scattering between sample and sample container in a more generic way than linear programs. However, this package was written for a few specific cases on specific instrumentation, creating difficulties in extending it to more sophisticated instrument configurations and sample assemblies.

MCViNE[32] is a general purpose neutron ray tracing package that combines the two different approaches. It is implemented in C++ and Python. At the

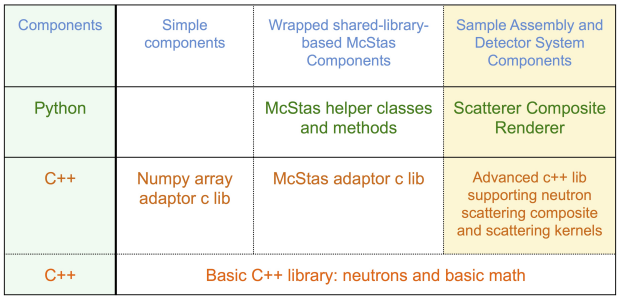


Figure 1: The MCViNE architecture is divided into three categories for serving different neutron ray-tracing components: simple NumPy-based components, McStas-based components, and components built with OOP principles for sample assemblies and detector systems. These categories are served by the vertical integration of three layers comprised of Python components at the top, followed by python libraries, then C++ libraries. The foundation of the MCViNE architecture is a C++ library with basic neutron objects and math functions.

C++ level, neutron ray tracing was implemented generically so that it can handle multiple scattering inherently. At the Python layer, however, MCViNE allows construction of a component chain for an instrument similar to the first class of neutron ray tracing packages. One effect of using Python components is that neutron packets are passed through the component chain in a group, to reduce the overhead of calling C/C++ functions from Python. Each group of neutrons is represented by an array.

Figure 1 depicts the architecture of the MCViNE package. Two layers of libraries exist in C++. The bottom layer is a basic C++ library that defines neutrons and some basic math facilities such as 3D vectors. Above this layer are three different types of C++ libraries: 1) A NumPy [45] array adaptor that allows a neutron group to be manipulated easily as a NumPy array at the Python level. 2) A McStas adaptor C library that provides support for MCViNE-wrapped McStas components. 3) An advanced C++ library that supports the concept of neutron scattering composite and scattering kernels, a unique feature of MCViNE. Above the three C/C++ libraries, a layer of Python helper classes and methods are implemented to provide a Python interface to the underlying C++ functionalities.

Three types of Python components sit on top of the Python adaption layer, including: 1) Simple, NumPy based neutron components, in which a group of neutron packets can be manipulated as a NumPy array. This makes it extremely easy to create simple neutron components, and to create prototypes of more sophisticated neutron components. 2) MCViNE-wrapped, shared-library-based McStas components. These components are McStas components, but compiled into shared libraries and bound to Python automatically by a MCViNE facility. Unlike simulations in McStas, however, MCViNE components are not compiled to a monolithic executable. 3) Components that use the notion of composite scatterer and scattering kernels. Currently two such components exist, one for

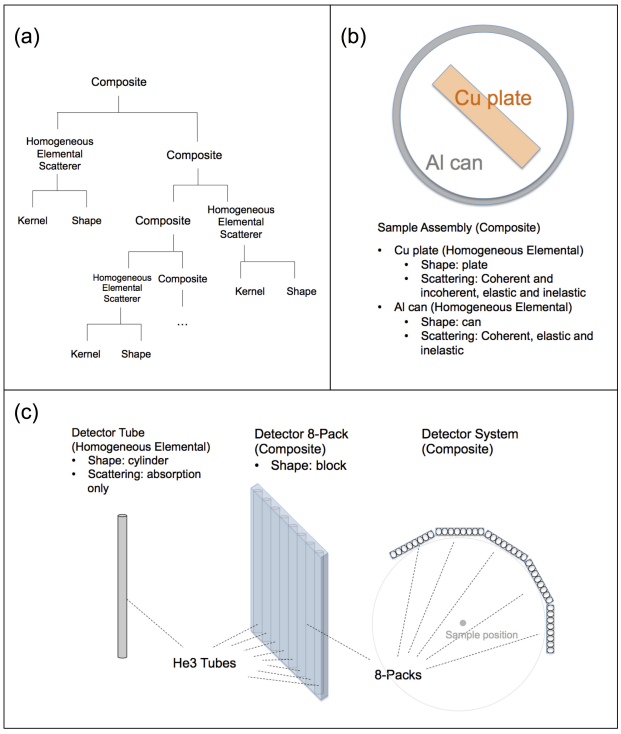


Figure 2: Concepts in scattering composites: composite scatterer, homogeneous scatterer, shape, scattering kernels. (a) an abstract hierarchy of an abitrary scattering composite. (b) and (c) are concrete examples of such hierarchies. (b) top view of a sample assembly consisting of an aluminum can and a copper plate. (c) a detector system – how it is constructed from an elemental scatterer (detector tube) in a three-level hierarchy.

sample assemblies and one for detector systems. The unique feature of MCViNE, the "composite scatterer", will be explained in detail in section 2.2.

Imperative programming is the predominant programming paradigm employed in MC neutron ray tracing programs. In imperative programming, different aspects of programming data and logic are tightly coupled. Object-oriented programming (OOP) is less used in scientific programming. Fundamental OOP concepts include encapsulation, polymorphism, dynamic dispatch, and delegation. These methods promote abstraction and decoupling of data and programming logic, result in codes that are more extensible, more maintainable, and easier to debug [33, 46, 47, 48]. It should be noted that runtime efficiency of a program is not the main focus of the OOP paradigm: to achieve polymorphism, for example, additional machine codes are generated by compilers to facilitate the dynamic dispatch by using the virtual table. OOP codes are harder to optimize by the compiler, too. It is not uncommon for OOP codes to run slower than programs written with imperative programming. This inefficiency, however, is overcome by tremendous improvements in both developer produc-

tivity and software sustainability. In the following we will show how some OOP concepts and design patterns are used in MCViNE and produce an extensible simulation framework.

### *2.2. Composite Scatterer*

In this section, basic concepts with regard to the "composite scatterer" are presented first, followed by details of the object-oriented software design centered around it. This section finishes with descriptions of some algorithms taking advantage of this software design.

#### *2.2.1. Concepts*

In MCViNE, a "composite neutron scatterer" represents a group of physical objects, for example, a powder sample in an aluminum can, a single crystal sample surrounded by a furnace, or a detector system. An "elemental scatterer" is a scatterer without constituent scatterers. A "homogeneous scatterer" is one kind of elemental neutron scatterer, whose scattering function is homogeneous within its volume. The scattering properties are modeled using one "scattering kernel" or a combination of several "scattering kernels", each of which represents one scattering mechanism, such as incoherent one-phonon nuclear scattering or coherent magnetic scattering.

These concepts are illustrated in Figure 2. Figure 2(a) is an example of an abstract hierarchy of a composite scatterer in MCViNE. In principle, the hierarchy in MCViNE can be arbitrarily deep. In practice, the depth of the hierarchy is limited by factors such as computing resources available for the simulations, and compiler limitations. Figure 2(b) depicts a sample assembly that is a composite of two-level hierarchy, in which the bottom level consists of two homogeneous elemental scatterers: one aluminum can and one copper plate sample. Figure 2(c) represents a detector system consisting of $^3$He eight-packs that form roughly a cylindrical arrangement around the sample position. The detector system is represented in MCViNE in a three-level hierarchy: at the bottom level is the $^3$He detector tube; at the middle level, 8 such tubes construct an 8-pack; at the top-level, the detector system consists of a collection of 8-packs. Such hierarchical representations allow MCViNE to model the physical reality closely.

#### *2.2.2. Object Oriented Design*

These concepts lead to one major design decision made in the MCViNE project: employment of the "composite" and "visitor" design patterns of object-oriented programming[33]. By using these design patterns for scattering composites, we can unify the programming interfaces to the operations on both the composites and the individual elemental objects. Composite and visitor patterns are used in three major aspects of the MCViNE neutron scattering model: the neutron scatterers, the geometric shapes of scatterers, and the scattering kernels.

**Neutron scatterers**. By using the composite pattern, algorithms for multiple scattering can be consolidated in one implementation. Scattering from a

composite neutron scatterer starts with a determination of which constituent intersects the incident neutron ray, and then delegates the scattering assessment to that particular constituent, which could be a composite itself that requires another delegation for scattering. The hierarchical representation of neutron scatterers and this recursive algorithm work for both samples and detector systems, and can improve computing efficiency and code maintenance.

**Geometric shapes** Using constructive solid geometry (CSG) (see, for example, [49]), composite shapes are constructed from primitives and composites by using operations such as union, intersection and difference. Ray-tracing through shapes is therefore simplified as visitor methods of the primitive shapes and the binary shape operations.

**Scattering kernels** Because the scattering kernel can be a composite, researchers can simulate slowly-varying $S(\mathbf{Q}, \omega)$, together with dynamical structure factors containing sharp features, such as diffraction and coherent phonon scatterings. Scattering kernels of similar nature can be grouped into a composite, and importance sampling can be realized by assigning different simulation weights to different kernels, either composite or elemental.

A "scattering kernel" in MCViNE is conceptually different from sample components in linear MC neutron ray tracing packages. A scattering kernel in MCViNE is an abstraction of the scattering mechanisms such as diffraction, nuclear scattering by phonons, and magnetic scattering by spin waves. It does not include the sample geometry but only the scattering physics. A sample component in earlier packages, on the other hand, includes both the geometry and the physics in one programming unit. By separating the implementation of "scatterer", "shape", and "scattering kernel", a sample in MCViNE can consist of a combination of scattering kernels. Furthermore, the scattering kernel library in the MCViNE framework can be extended without affecting the logic of geometric ray tracing, which is implemented in "shape" and "scatterer". For example, for isotropic scattering, scattering kernels taking a histogram form of $S(Q, \omega)$ can be supported, as well as phonon scattering kernels taking phonon energies and polarizations as inputs (examples are given in Section 3.1 and 3.2). A scattering kernel conveniently taking the analytical form of a dispersion can be used (see [9] for an example) to improve convergence (effective when combined with other scattering kernels), and to avoid unnecessary broadenings resulted from approximating $S(Q, \omega)$ using a histogram. Inelastic and elastic scattering kernels for single crystals can also be developed to simulate single crystal experiments.

#### *2.2.3. Algorithms*

In this section, implementation of multiple scattering and ray tracing in detector systems are presented as algorithm examples that benefit from the conceptual analysis and the software design.

**Multiple Scattering**

Multiple-scattering (MS) is naturally supported in MCViNE scattering composites, implemented with a recursive algorithm. MCViNE differentiates between two types of multiple scattering, single-scatterer multiple scattering (SSMS)

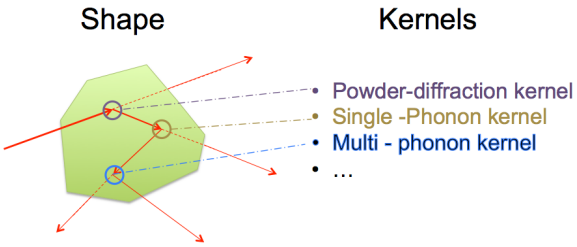


Figure 3: An example of multiple scattering within one scatterer. The incident neutron was scattered three times by three different scattering kernels. At each scattering point, the original neutron is also propagated out of the scatterer with proper attenuation. Red arrows are paths of neutron propagation. Circles highlight the location of scattering. Different scattering events are coded using different colors.

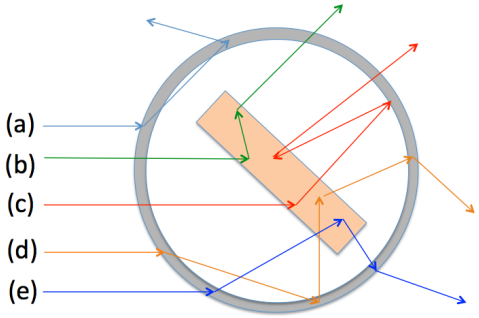


Figure 4: An example of multiple scattering in a concentric sample assembly. Five (out of infinite) possible multiple scattering paths are illustrated.

to describe the multiple scattering within one neutron scatterer and multiple-scatterer multiple scattering (MSMS) to describe multiple scattering among neutron scatterers.

Figure 3 shows an example of SSMS in which a neutron gets scattered three times before exiting a scatterer. Each time a neutron is scattered inside a homogeneous scatterer, the original incident neutron packet is split into two neutron packets for computational efficiency. One neutron packet is propagated through the scatterer with its probability lowered by attenuation, while the other is scattered by one of the scattering kernels, chosen by a random selection, at a point also randomly selected along the forward path of the incident neutron. This splitting process repeats for the scattered neutron several times, as illustrated in Figure 3, until either the neutron probability is lower than a pre-selected limit, or the maximum order of multiple scattering is reached. At this point, the neutron that is still inside the scatterer is allowed to propagate out, with its probability attenuated appropriately.

Figure 4 shows an example of multiple scattering in a sample assembly con-

sisting of a "concentric" arrangement of a sample and a sample environment. Only five of an infinite number of possible multiple scattering paths are illustrated, and the splitting processes are not shown to avoid cluttering.

The multiple scattering algorithm of MCViNE is generic, and it can handle more complex sample assemblies, such as non-concentric arrangements, and mixing of non-concentric and concentric arrangements. More details about the MS algorithm of MCVINE can be found in the supplemental material for this paper.

Sample components in some linear-chain-based MC ray tracing packages can support SSMS, but they do not have abstractions similar to composite scatterer or scattering kernel. As a result, the SSMS algorithm must be duplicated in these sample components, while in MCViNE, implementations of new scattering kernels can be added without reimplementing the multiple scattering algorithm. McStas supports MSMS partially for a concentric sample assembly by, for example, adding a second outer cylinder into the simulation component chain [50]. Path (e) of Figure 4 is included this way, but path (c) of Figure 4 is not. Other ways of simulating MSMS may be possible with McStas, but these would require significant more effort on the user's part.

The multiple scattering algorithm of MCViNE is more comparable to that of MSCAT[11] in which the sample and the sample environment are treated together in the multiple scattering loop, offering complete treatment of SSMS and MSMS. However, MCViNE allows a straightforward increase in complexity of the sample and sample environment interactions by using the recursive MS algorithm enabled by OOP. MSCAT by default only allows for a few specific arrangements. MSCAT and some McStas components contain the ability to appropriately transform the angular scattered distribution off of the sample so as to only simulate neutrons that will impact the detector, such optimization is not yet available in MCViNE.

**Ray tracing in a detector system**

Ray tracing of a neutron through a sophisticated detector system in instruments such as ARCS and SEQUOIA, where flat detector packs are arranged in an approximately cylindrical arrangement, illustrates another strength of the software design of MCViNE. MCViNE takes advantage of the hierarchical representation for neutron scatterers, only in this case the elemental homogeneous neutron scatterer is the $^3$He detector tube that intercepts neutrons and records them. MCViNE reuses the code for ray tracing in a composite scatterer for simulating $^3$He detector systems, and the new code needed is a scattering kernel for the $^3$He material that takes into account gas absorption. The ray tracing through a cylinder takes care of the parallax and border effect of the detector tube. When a neutron is sent to a detector system shown in Figure 2(c), for example, the generic ray tracing algorithm for composite scatterers first checks whether the top level composite scatterer is penetrated by the neutron. If so, all constituents of the composite scatterer, i.e. the detector packs, are examined to determine which of them intercepts the neutron. Unless a neutron traverses a gap between detector packs, the detector pack is identified and then its constituents, the 8 detector tubes, are examined for neutron detection. The path

of a neutron through the detector tube is then computed by ray tracing of the neutron through a cylinder, and a MC sampling picks a point in the path for the neutron to be absorbed. The position in the tube is used to calculate a unique pixel identifier known as the Pixel ID, according to the scheme readable by the Mantid software framework [51, 52]. Additionally, the appropriate weighting multiplier for neutron probability (computed from absorption probability depending on the $^3$He pressure and the length of the neutron path through the tube) and the time-of-flight are computed for the neutron to be recorded as a detector event in a "virtual detector electronics device". Our hierarchical approach to detectors allows for the addition of as much detail as necessary, including details of the charge cloud and the wire.

## 3. Examples

This section presents examples of MCViNE simulations performed for experiments on the ARCS[53], SEQUOIA[54, 55], and HYSPEC[56] instruments at the Spallation Neutron Source (SNS). Every simulation consists of 4 steps:

**Beam simulation.** The incident beams on the sample for ARCS SEQUOIA, and HYSPEC instruments were simulated. The simulation applications were derived from the McStas[12] instrument definitions used in the design phase of the instruments[44, 54, 57, 58]. In this work, $10^9$ neutron events emitted from the moderator were included in all the simulations, and the neutrons at the sample position were saved and reused in the next step.

**Sample scattering.** The neutron packets saved in the previous step were sent to a SampleAssembly component. The scattered neutrons were then saved.

**Detector interception.** Each neutron scattered by the sample was processed by a DetectorSystem component and an event was recorded in an event-mode NeXus file if it intercepted a detector tube. In ray-tracing through a detector system, the detector tube in which the event was detected was located using a hierarchical set of detector tubes as described previously, while the exact location and time-of-flight were determined by a MC selection.

**Reduction.** The NeXus data generated in the previous step were reduced using Mantid[51, 52]. The only difference between the simulated and measured data is that the intensities in the simulations are computed as the sum of the probabilities of all packets arriving in the bin of interest, while those in the data are total event counts. The data reduction workflow is therefore identical, and uses the same code base for both the simulated and the measured data. The goal of this four-step simulation process was to reproduce the experiment (including data reduction) by a simulation of high fidelity.

This 4-step simulation workflow produces output files such as the simulated scattered neutrons, the simulated event-mode NeXus file, and the reduced $I(Q, E)$ file.

The simulation examples here make use of the following scattering kernels, described briefly in the Supplemental Material:

- incoherent elastic scattering

- coherent elastic scattering from powder sample
- incoherent inelastic single-phonon scattering
- coherent inelastic single-phonon scattering from a powder sample
- multi-phonon scattering
- scattering from a dispersion surface where the dispersion relation and the dynamical structure factor are described by analytical functions of momentum transfer vector $\mathbf{Q}$

Three examples are presented in the following subsections, two modeling vibrational excitations, and one modeling magnetic excitations. The simplest sample, a vanadium plate, is presented first in Subsection 3.1, where only incoherent scattering kernels are used. Coherent phonon scattering kernels for powder samples are introduced for an aluminum sample in Subsection 3.2. Both Subsection 3.1 and 3.2 demonstrate the ability to easily turn on and off different scattering mechanisms, allowing researchers to gain a better understanding of their contributions. Subsection 3.3 presents a simulation of a measurement on a single-crystal $K_2V_3O_8$ sample, for which a dispersion-surface scattering kernel is used.

In addition to these three examples, MCViNE simulations of Uranium Nitride measurements performed on the ARCS and SEQUOIA instruments provide an excellent example of the capabilities presented here [9]. In this case, the UN sample exhibited particularly strong multiple scattering due to its size. MCViNE simulations were able to reproduce well the multiple scattering, identified weak scattering from accoustic phonons, and showed that the binary solid model is a good explanation of the temperature-dependent broadening of the modes of the quantum harmonic oscillator [9].

### *3.1. Vanadium*

Here, we present experimental and simulated inelastic spectra for a vanadium plate sample (5cm×5cm×1.2mm) in the ARCS instrument. In the experiment, the sample was approximately perpendicular to the beam, the incident energy was tuned to about 120meV using a Fermi chopper with 1.5mm slit spacing, rotating at 600Hz. In the simulation, the incident beam was at ∼117meV with the Fermi chopper choice matching the experimenal one. The sample assembly contains only one homogeneous scatterer for the vanadium plate, which was tilted 96.6 degrees from the beam direction. Different scattering kernels were used for different simulations, but one incoherent elastic kernel and one single-phonon incoherent inelastic kernel were included for all. All phonon-releated scattering kernels use the phonon density of states (DOS) calculated from a Born-von Karman (BvK) model [59]. Only one universal scale factor was applied to the intensities of all simulated spectra to match the experimental data.

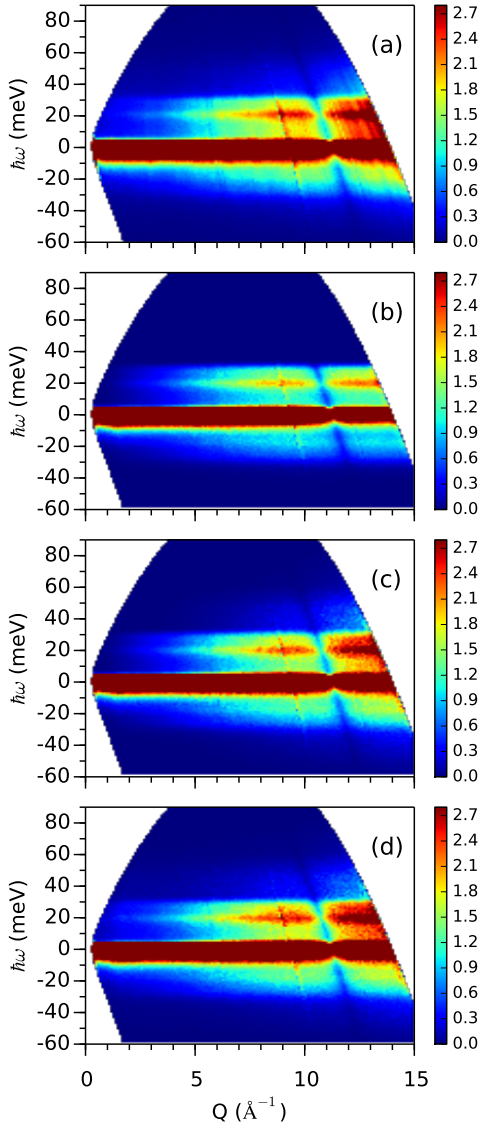


Figure 5: $I(Q, \omega)$ plots of vanadium inelastic spectra obtained from experiment and simulations for a vanadium plate at room temperature in the ARCS instrument. (a) Experiment (b) Simulation without a multi-phonon kernel. Multiple scattering was turned off. (c) Simulation with a multi-phonon kernel. Multiple scattering was turned off. (d) Simulation with a multi-phonon kernel. Multiple scattering was turned on.

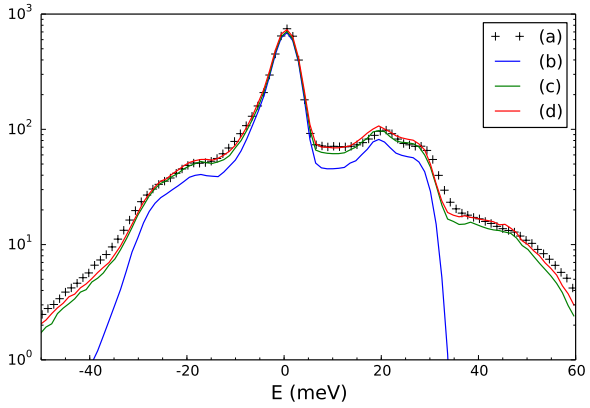


Figure 6: Energy spectra integrated over Q range (8,12) inverse angstrom, obtained from experiment and simulations for a vanadium plate placed in the ARCS beam. The intensity axis is in log scale. (a)-(d) same as Figure 5

Shown in Figure 5 are $I(Q,\omega)$ plots. The top panel is the experimental result. Panel (b) was simulated without either multi-phonon scattering or multiple-scattering. Panel (c) was simulated with multi-phonon scattering but multiple-scattering was turned off. Comparing (b) and (c), we can see how multi-phonon scattering contributes to intensities at high $Q$ (12-14 inverse Å), especially noticeable at high energy transfer near $E = 40$meV. Panel (d) was done with both multi-phonon and multiple-scattering contributions. Comparing (c) and (d) shows how the effects of the multiple scattering are small in this case. This is understandable because the plate is very thin. It also shows that there is less $Q$-dependence in multiple-scattering than in multi-phonon scattering.

Figure 6 shows the energy spectra integrated over momentum transfer range of 8 to 12 $\text{Å}^{-1}$ in log scale. Similarly, we found that multi-phonon scattering contribute more substantially than multiple scattering in this experiment.

### *3.2. Aluminum*

In this example, we present experimental and simulated inelastic spectra from a polycrystalline aluminum plate (6cm×6cm×4mm) in the ARCS instrument. In the experiment, the sample was placed approximately at 135 degrees from the beam. The incident energy was tuned to ∼80meV using the 1.5mm slit spacing Fermi chopper spinning at 480Hz. In the simulation, the incident beam was at ∼80.5meV, with the Fermi chopper choice matching the experimenal one. The sample assembly contains only one homogeneous scatterer for the aluminum plate. Different simulations made use of different combinations of scattering kernels. All phonon-related scattering kernels use phonon energies and polarization vectors computed on a regular grid in a Brillouin zone from a BvK model [60]. The broadening of the phonon modes was not included. Only

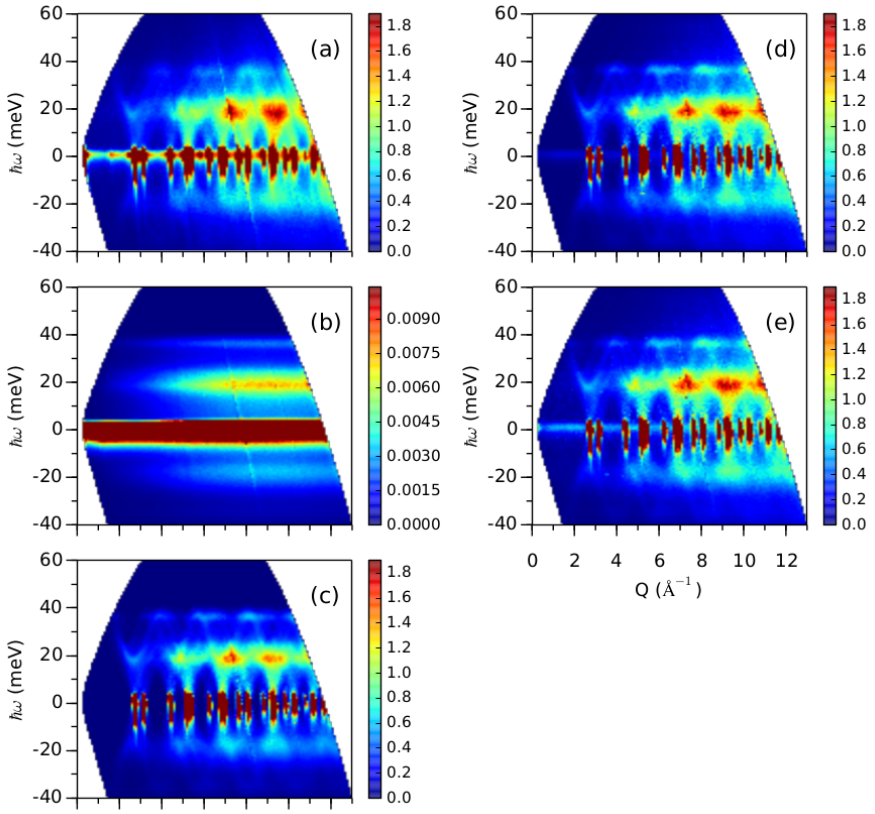


Figure 7: $I(Q, \omega)$ plots of aluminum inelastic spectra obtained from experiment (a) and simulations (b)-(e) of an aluminum plate at room temperature in the ARCS instrument. Scattering kernels included in the simulations are (b) incoherent elastic and incoherent inelastic single-phonon scattering (see note on intensity scaling in text), (c) coherent elastic (powder diffraction) and coherent inelastic single-phonon scattering, (d) all kernels included in (b) and (c) plus a multi-phonon kernel using an incoherent approximation and (e) all kernels included in (d) plus multiple scattering.

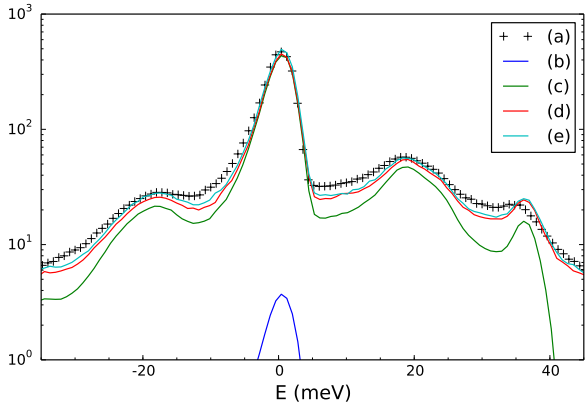


Figure 8: Energy spectra integrated over Q range (6,10) inverse angstrom, obtained from experiment and simulations for an aluminum plate placed in the ARCS beam. The intensity axis is in log scale. (a)-(e) same as Figure 7

one universal scale factor was applied to all simulated spectra to match the experimental data.

Figure 7 shows $I(Q, \omega)$ plots for the aluminum plate. The experimental result is given in panel (a) and panels (b)-(e) show simulated data. In (b) only the incoherent elastic and incoherent single phonon scattering are included. In this plot the maximum intensity for the color scale is reduced by the ratio of incoherent/coherent cross sections of aluminum, so one can see the details in the plot. Nevertheless the numerical values on the colorbar give an indication of the scaling. In (c) only the coherent elastic (powder diffraction) and the coherent single-phonon inelastic scattering are included. In (d), all of the kernels in (b) and (c) with the addition of a multi-phonon kernel using the incoherent approximation. In (e), all of the kernels in (d) are used with multiple scattering turned on. Overall the features shown in the experiment data (a) and the simulated data (e) agree very well. Comparison of (b) and (c) shows that coherent scattering gives rise to more features such as diffraction peaks and phonon dispersions. It is evident from comparing (c) and (d) that multiphonon scattering increases in intensity at higher $Q$. The most obvious difference in (d) and (e) is in the elastic line, which shows that multiple scattering seems to contribute similarly to incoherent elastic scattering. The elastic lines in (a) and (e) seem to show that the sample used in the experiment may contain traces of an additional phase, most likely from a surface layer of $Al_2O_3$.

Figure 8 shows the energy spectra integrated over momentum transfer range of 6 to 10 $Å^{-1}$ in log scale. Similarly, we found that multi-phonon scattering contributes more substantially than multiple scattering in this experiment. The small discrepancy between the experimental data (curve (a)) and the simulated data (with all kernels, curve (e)) was expected, because the broadening of Al phonon modes [61, 62] was not taken into account in our simulation, and perhaps

because the BvK model used was deduced from phonon dispersions measured along only the [100], [110], and [111] directions[60].

### *3.3. $K_2V_3O_8$ single crystal*

We now present experimental and simulated inelastic single-crystal spectra for a $K_2V_3O_8$ sample measured at the HYSPEC instrument, a hybrid spectrometer at SNS [56]. The sample consisted of 5 co-aligned crystals with an overall cylindrical shape approximately 1.5 inch in diameter and 1 inch in height. The sample was oriented so that at zero degrees of rotation angle its [100] direction was along the beam and its [001] direction pointed upward vertically. Measurements were performed at 1.5 K with an incident energy of ∼7meV with a Fermi chopper frequency of 180Hz. The detector vessel was oriented so that neutrons scattered from the sample in the horizontal plane were measured in the scattered angle range of -75 to -15 degrees. To span reciprocal space, the goniometer angle was swept from 40 to -50 degrees in 0.5 degree steps and then from -50 to -28 degrees in 1 degree steps.

The simulation was done for a scan matching the experimental setup. The sample assembly contains one homogeneous scatterer for the $K_2V_3O_8$ sample with a shape matching the overall shape of the sample in the experiment. Two scattering kernels were included in the simulation: one incoherent elastic scattering kernel to approximate the elastic line, and one dispersion-surface scattering kernel for simulating the scattering from the spin-wave.

In $K_2V_3O_8$ the long-wavelength spin-wave dispersion is well described by a result for the quantum (S=1/2) square lattice Heisenberg antiferromagnet [63]:

$$E(\mathbf{Q}) = 2\tilde{J}\sqrt{1-\gamma_{Q_{//}}^2} \tag{1}$$

with the dynamic structure factor

$$S(\mathbf{Q},E) = \frac{1-\gamma_{Q_{//}}}{2\sqrt{1-\gamma_{Q_{//}}^2}}\,\delta(E-E(\mathbf{Q})) \tag{2}$$

where $\gamma_{Q_{//}} = \cos(h\pi)\cos(k\pi)$, $2\tilde{J} = 2.563$. The differential cross section is

$$\left(\frac{d^2\sigma}{d\Omega dE_f}\right) \sim \frac{k_f}{k_i}\;|F(Q)|^2\,[n(E)+1](1+\cos^2\phi)S(\mathbf{Q},E) \tag{3}$$

where $k_i$ and $k_f$ are the magnitudes of the incident and final neutron wave vectors, $F(Q)$ is the magnetic form factor for $V^{4+}$ [64], $n(E)+1$ is the Bose occupation factor, and $1+\cos^2\phi$ is a polarization term ($\phi$ is the angle between $\mathbf{Q}$ and the easy c-axis).

In treatment of both experimental and simulated data, Mantid was used to reduce the measured NeXus file to NXSPE format at each goniometer angle, and then a Python program was used to project data in NXSPE files to the four dimensional $\mathbf{Q}$, $E$ space. Slices along desired $\mathbf{Q}$ directions could then be taken.

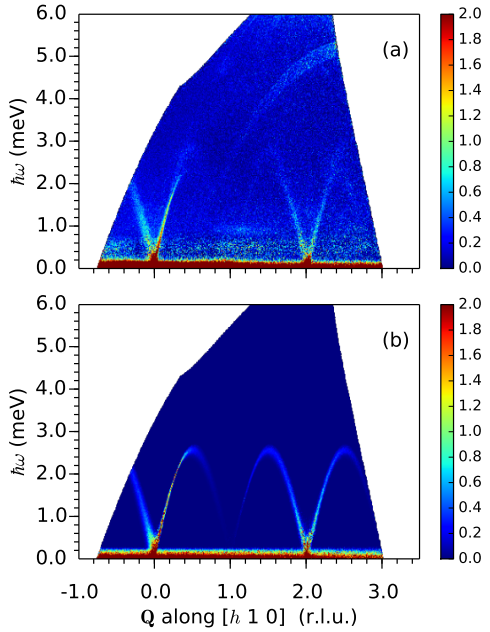


Figure 9: Slices along the $\mathbf{Q}$=[$h$10] axis and the energy axis from (a) experiment and (b) simulation, taken in the range $l$=(-0.3, 0.3) and $k$=(0.93,1.07).

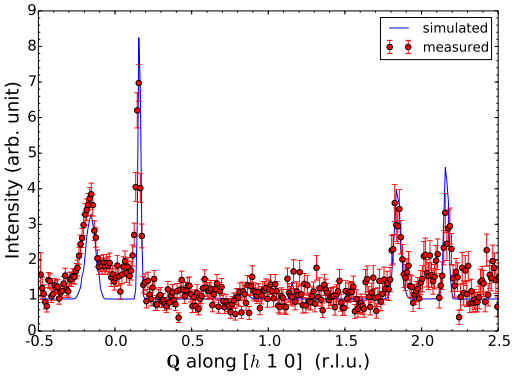


Figure 10: Constant energy cuts of the slices as shown in Figure 9 in the energy range of [1.2, 1.3] meV. A constant background was added to the simulated data for comparison.

Shown in Figure 9 are experimental and simulated slices along axes of $\mathbf{Q} = [h10]$ and energy. The spin wave dispersion in the energy range between $\sim$0.3 and $\sim$2.1 meV shows good agreement between experimental and simulated data. In the experimental data, the noise in the energy range of [0.25, 0.7] is higher than the noise at higher energies. This is due to elastic scattering from the cryostat, which was subtracted from the data. Both plots show a distinctive feature – for the dispersion near [010] the right branch is sharper than the left branch, while the dispersion branches near [210] are largely symmetric in their broadening. This effect is more clear in Figure 10, where constant-energy cuts over [1.2, 1.3] meV are plotted against $\mathbf{Q} = [h10]$ for the experimental (circles with error bars) and the simulated (solid line) intensities. Both the experimental data and simulated data show that the peak near $h = 0.15$ is much sharper than that near $h = -0.15$. Such an effect is expected due to diffrent focusing conditions of the resolution ellipsoid [65, 66]. The spin-wave dispersion above $\sim$2.1meV ($h \sim 0.33$, for example) has weaker intensity in the experimental data than expected from the simulated data, which could be attributed to mode splitting near the zone boundary [63].

## 4. Conclusions

The MCViNE software package for Monte Carlo neutron ray tracing simulations is based on modern object-oriented software design that decomposes neutron scatterers into a hierarchy of composite and elemental scatterers. This software design elegantly solves algorithmic problems including multiple scattering in a sample assembly, and ray tracing in a sophisticated detector system. Multiple scattering and instrument resolution are included naturally in MCViNE simulations, and simulation of ray-tracing in a complex detector system such as those of the ARCS and SEQUOIA instruments is straightforward. Adding, removing, and modifying scattering kernels in the simulations can help show the contributions of different types of scattering events to the experimental data. The examples of scattering from vibrational and magnetic excitations presented here and elsewhere[9] demonstrate that such simulations can improve our understanding of the underlying physics of neutron spectra.

MCViNE is an open source software and is freely available for the Linux platform. More details about the conditions of use and license can be found at http://danse.us/trac/MCViNE/wiki/license. Details on build and installation, usage, source repository, and user support of MCViNE are available in the documentation [32]. Feedback to the MCViNE developers can be provided through the MCViNE user mailing list http://groups.google.com/group/mcvine-users.

## Acknowledgements

The development of the MCViNE software was begun by J.Y.Y.L. under the DANSE project supported by the NSF award DMR-0520547. The research on simulations of experiments in the ARCS, SEQUOIA, and HYSPEC instruments was supported by the U.S. Department of Energy, Office of Basic Energy

Sciences. G.E.G., A.A.A., D.L.A., M.D.L., B.A. were fully supported, J.Y.Y.L. and H.L.S. partially supported by the Scientific User Facilities Division. We thank M. E. Hagen and P. Willendrup for stimulating discussions. We also thank L. Li and A. Dementsov for developing the powder diffraction scattering kernel for MCViNE, A. Fang for building MCViNE adaptations of some McStas components, and M. Reuter and S. Campbell for updating the MANTID code to read in the Monte Carlo generated data.

## References

[1] V. Hugouvieux, E. Farhi, M. R. Johnson, F. Juranyi, P. Bourges, W. Kob, Structure and dynamics of l-ge: Neutron scattering experiments and ab initio molecular dynamics simulations, Phys. Rev. B 75 (2007) 104208. doi:10.1103/PhysRevB.75.104208.
URL http://link.aps.org/doi/10.1103/PhysRevB.75.104208

[2] A. C. Walters, T. G. Perring, J.-S. Caux, A. T. Savici, G. D. Gu, C.-C. Lee, W. Ku, I. A. Zaliznyak, Effect of covalent bonding on magnetism and the missing neutron intensity in copper oxide compounds, Nature Physics 5 (12) (2009) 867–872.

[3] O. Delaire, K. Marty, M. B. Stone, P. R. Kent, M. S. Lucas, D. L. Abernathy, D. Mandrus, B. C. Sales, Phonon softening and metallization of a narrow-gap semiconductor by thermal disorder, Proceedings of the National Academy of Sciences 108 (12) (2011) 4725–4730.

[4] F. Weber, S. Rosenkranz, L. Pintschovius, J.-P. Castellan, R. Osborn, W. Reichardt, R. Heid, K.-P. Bohnen, E. Goremychkin, A. Kreyssig, et al., Electron-phonon coupling in the conventional superconductor yni 2 b 2 c at high phonon energies studied by time-of-flight neutron spectroscopy, Physical review letters 109 (5) (2012) 057001.

[5] A. A. Aczel, G. E. Granroth, G. J. MacDougall, W. J. L. Buyers, D. L. Abernathy, G. D. Samolyuk, G. M. Stocks, S. E. Nagler, Quantum oscillations of nitrogen atoms in uranium nitride, Nature Communications 3 (2012) 1124.

[6] S. E. Hahn, A. A. Podlesnyak, G. Ehlers, G. E. Granroth, R. S. Fishman, A. I. Kolesnikov, E. Pomjakushina, K. Conder, Inelastic neutron scattering studies of yfeo$_3$, Phys. Rev. B 89 (2014) 014420. doi:10.1103/PhysRevB.89.014420.
URL http://link.aps.org/doi/10.1103/PhysRevB.89.014420

[7] K. W. Plumb, A. T. Savici, G. E. Granroth, F. C. Chou, Y.-J. Kim, High-energy continuum of magnetic excitations in the two-dimensional quantum antiferromagnet sr$_2$cuo$_2$cl$_2$, Phys. Rev. B 89 (2014) 180410. doi:10.1103/PhysRevB.89.180410.
URL http://link.aps.org/doi/10.1103/PhysRevB.89.180410

[8] C. W. Li, O. Hellman, J. Ma, A. F. May, H. B. Cao, X. Chen, A. D. Christianson, G. Ehlers, D. J. Singh, B. C. Sales, O. Delaire, Phonon self-energy and origin of anomalous neutron scattering spectra in snte and pbte thermoelectrics, Phys. Rev. Lett. 112 (2014) 175501. doi:10.1103/PhysRevLett.112.175501.
URL http://link.aps.org/doi/10.1103/PhysRevLett.112.175501

[9] J. Y. Y. Lin, A. A. Aczel, D. L. Abernathy, S. E. Nagler, W. J. L. Buyers, G. E. Granroth, Using monte carlo ray tracing simulations to model the quantum harmonic oscillator modes observed in uranium nitride, Phys. Rev. B 89 (2014) 144302. doi:10.1103/PhysRevB.89.144302.
URL http://link.aps.org/doi/10.1103/PhysRevB.89.144302

[10] F. G. Bischoff, Generalized monte carlo methods for multiple scattering problems in neutron and reactor physics, Ph.D. thesis, Rensselaer Polytechnic Institute (1970).

[11] J. R. D. Copley, P. Verkerk, A. A. Van Well, H. Fredrikze, Improved monte carlo calculation of multiple scattering effects in thermal neutron scattering experiments, Computer Physics Communications 40 (2) (1986) 337–357.

[12] K. Lefmann, K. Nielsen, Mcstas, a general software package for neutron ray-tracing simulations, Neutron News 10 (3) (1999) 20–23.

[13] P. Willendrup, E. Farhi, K. Lefmann, Mcstas 1.7 - a new version of the flexible monte carlo neutron scattering package, Physica B: Condensed Matter 350 (13, Supplement) (2004) E735 – E737, proceedings of the Third European Conference on Neutron Scattering. doi:http://dx.doi.org/10.1016/j.physb.2004.03.193.
URL http://www.sciencedirect.com/science/article/pii/S0921452604004144

[14] G. Zsigmond, K. Lieutenant, F. Mezei, Monte carlo simulations of neutron scattering instruments by vitess: Virtual instrumentation tool for ess, Neutron News 13 (4) (2002) 11–14. arXiv:http://www.tandfonline.com/doi/pdf/10.1080/10448630208218488, doi:10.1080/10448630208218488.
URL http://www.tandfonline.com/doi/abs/10.1080/10448630208218488

[15] W.-T. Lee, X.-L. Wang, J. Robertson, F. Klose, C. Rehm, Ideas a monte carlo simulation package for neutron-scattering instrumentation, Applied Physics A 74 (1) (2002) s1502–s1504. doi:10.1007/s003390201723.
URL http://dx.doi.org/10.1007/s003390201723

[16] L. L. Daemen, P. A. Seeger, R. P. Hjelm, T. G. Thelliez, Monte carlo tool for neutron optics and neutron scattering instrument design, SPIE Proc. 3771.

[17] T. Proffen, R. Neder, Discus: A program for diffuse scattering and defect-structure simulation, Journal of applied crystallography 30 (2) (1997) 171–175.

[18] T. Proffen, R. Neder, Discus, a program for diffuse scattering and defect structure simulations-update, Journal of Applied Crystallography 32 (4) (1999) 838–839.

[19] T. Proffen, R. Neder, DISCUS.
URL http://discus.sourceforge.net/

[20] J. Šaroun, J. Kulda, Restrax - a program for tas resolution calculation and scan profile simulation, Physica B: Condensed Matter 234 (1997) 1102–1104.

[21] J. Šaroun, J. Kulda, RESTRAX.
URL http://neutron.ujf.cas.cz/restrax/

[22] V. Hugouvieux, E. Farhi, M. Johnson, W. Kob, Virtual neutron scattering experiments, Physica B: Condensed Matter 350 (13) (2004) 151 – 154, proceedings of the Third European Conference on Neutron Scattering. doi:http://dx.doi.org/10.1016/j.physb.2004.04.015.
URL http://www.sciencedirect.com/science/article/pii/S0921452604005769

[23] L. Udby, P. K. Willendrup, E. Knudsen, C. Niedermayer, U. Filges, N. B. Christensen, E. Farhi, B. Wells, K. Lefmann, Analysing neutron scattering data using mcstas virtual experiments, Nuclear Instruments and Methods in Physics Research Section A: Accelerators, Spectrometers, Detectors and Associated Equipment 634 (1) (2011) S138–S143.

[24] P. L. Tregenna-Piggott, F. Juranyi, P. Christiansen, P. K. Willendrup, K. Lefmann, Reduction of data from inverted-geometry time-of-flight instruments, Journal of Neutron Research 16 (1-2) (2008) 13–22.

[25] M. Boin, A. Hilger, N. Kardjilov, S. Zhang, E. Oliver, J. James, C. Randau, R. Wimpory, Validation of bragg edge experiments by monte carlo simulations for quantitative texture analysis, Journal of Applied Crystallography 44 (5) (2011) 1040–1046.

[26] M. Boin, nxs: a program library for neutron cross section calculations, Journal of Applied Crystallography 45 (3) (2012) 603–607.

[27] K. Lefmann, P. K. Willendrup, L. Udby, B. Lebech, K. Mortensen, J. O. Birk, K. KlenØ, E. Knudsen, P. Christiansen, J. Saroun, et al., Virtual experiments: the ultimate aim of neutron ray-tracing simulations, Journal of Neutron Research 16 (3-4) (2008) 97–111.

[28] E. Farhi, V. Hugouvieux, M. R. Johnson, W. Kob, Virtual experiments: Combining realistic neutron scattering instrument and sample simulations, Journal of Computational Physics 228 (14) (2009) 5251–5261.

[29] Farhi, E., Willendrup, P., Virtual experiments in a nutshell: Simulating neutron scattering from materials within instruments with mcstas, Collection SFN 12 (2011) 303–339. doi:10.1051/sfn/201112015.
URL http://dx.doi.org/10.1051/sfn/201112015

[30] P. K. Willendrup, L. Udby, E. Knudsen, E. Farhi, K. Lefmann, Using mcstas for modelling complex optics, using simple building bricks, Nuclear Instruments and Methods in Physics Research Section A: Accelerators, Spectrometers, Detectors and Associated Equipment 634 (1) (2011) S150–S155.

[31] E. Farhi, C. Monzat, R. Arnerin, T. van Vuure, C. Castán-Guerrero, C. Hennane, P. Harraud, G. Campioni, S. Fuard, J. Ollivier, et al., Advanced sources and optical components for the mcstas neutron scattering instrument simulation package, Journal of Neutron Research 17 (1) (2014) 63–74.

[32] J. Y. Y. Lin, M. A. Aivazis, B. Fultz, MCViNE.
URL http://docs.danse.us/MCViNE

[33] E. Gamma, R. Helm, R. Johnson, J. Vlissides, Design Patterns: Elements of Reusable Object-oriented Software, Addison-Wesley Longman Publishing Co., Inc., Boston, MA, USA, 1995.

[34] B. Fultz, et al., DANSE.
URL http://danse.us

[35] S. Kynde, K. H. Kleno, G. Nagy, K. Mortensen, K. Lefmann, J. Kohlbrecher, L. Arleth, A compact time-of-flight SANS instrument optimised for measurements of small sample volumes at the European Spallation Source, NUCLEAR INSTRUMENTS & METHODS IN PHYSICS RESEARCH SECTION A-ACCELERATORS SPECTROMETERS DETECTORS AND ASSOCIATED EQUIPMENT 764 (2014) 133–141. doi:{10.1016/j.nima.2014.06.084}.

[36] E. B. Klinkby, E. B. Knudsen, P. K. Willendrup, B. Lauritzen, E. Nonbol, P. Bentley, U. Filges, Application of the MCNPX-McStas interface for shielding calculations and guide design at ESS, in: Ioffe, A (Ed.), INTERNATIONAL WORKSHOP ON NEUTRON OPTICS AND DETECTORS (NOP&D 2013), Vol. 528 of Journal of Physics Conference Series, Forschungszentrum Julich GmbH, Julich Ctr Neutron Sci; European Spallat Source Scandinavia; Swiss Neutron; Mirotron Ltd; S DH Heidelberg; ASTRIUM, 2014, International Workshop on Neutron Optics and Detectors (NOP&D), Munich, GERMANY, JUL 02-05, 2013. doi:{10.1088/1742-6596/528/1/012032}.

[37] M. Bertelsen, H. Jacobsen, U. B. Hansen, H. H. Carlsen, K. Lefmann, Exploring performance of neutron guide systems using pinhole beam extraction, Nuclear Instruments and Methods in Physics Research Section A: Accelerators, Spectrometers, Detectors and Associated Equipment 729 (0) (2013) 387 – 398. doi:http://dx.doi.org/10.1016/j.nima.2013.07.062.
URL http://www.sciencedirect.com/science/article/pii/S0168900213010747

[38] O. Prokhnenko, K. Lieutenant, L. D. Cussen, W. D. Stein, C. Zendler, K. Prokes, Probing static and dynamic correlations in matter under extreme conditions: Concept of multi-purpose instrument at the European Spallation Source, NUCLEAR INSTRUMENTS & METHODS IN PHYSICS RESEARCH SECTION A-ACCELERATORS SPECTROMETERS DETECTORS AND ASSOCIATED EQUIPMENT 764 (2014) 30–41. doi:{10.1016/j.nima.2014.07.013}.

[39] A. Houben, W. Schweika, T. Brckel, R. Dronskowski, New neutron-guide concepts and simulation results for the {POWTEX} instrument, Nuclear Instruments and Methods in Physics Research Section A: Accelerators, Spectrometers, Detectors and Associated Equipment 680 (0) (2012) 124 – 133. doi:http://dx.doi.org/10.1016/j.nima.2012.03.015.
URL http://www.sciencedirect.com/science/article/pii/S0168900212002872

[40] M. Skoulatos, K. Habicht, Upgrade of the primary spectrometer of the cold triple-axis spectrometer {FLEX} at the {BER} {II} reactor, Nuclear Instruments and Methods in Physics Research Section A: Accelerators, Spectrometers, Detectors and Associated Equipment 647 (1) (2011) 100 – 106. doi:http://dx.doi.org/10.1016/j.nima.2011.05.037.
URL http://www.sciencedirect.com/science/article/pii/S016890021100948X

[41] Z. Izaola, M. Russina, Virtual design of the neutron guide for the tof spectrometer neat, Journal of Physics: Conference Series 251 (1) (2010) 012064.
URL http://stacks.iop.org/1742-6596/251/i=1/a=012064

[42] L. Alianelli, N. Wilson, K. Andersen, M. S. del Ro, R. Felici, A method for detailed simulations of neutron diffraction from imperfect crystals, Nuclear Instruments and Methods in Physics Research Section A: Accelerators, Spectrometers, Detectors and Associated Equipment 529 (13) (2004) 231 – 233, proceedings of the Joint Meeting of the International Conference on Neutron Optics (NOP2004) and the Third International Workshop on Position-Sensitive Neutron Detectors (PSND2004). doi:http://dx.doi.org/10.1016/j.nima.2004.04.161.
URL http://www.sciencedirect.com/science/article/pii/S0168900204009039

[43] A. Wildes, J. Saroun, E. Farhi, I. Anderson, P. Hoghoj, A. Brochier, A comparison of monte-carlo simulation programs with experiment: the effect of a focusing guide on resolution, Applied Physics A 74 (1) (2002) s1452–s1454. doi:10.1007/s003390101243.
URL http://dx.doi.org/10.1007/s003390101243

[44] G. E. Granroth, D. L. Abernathy, Performance comparisons of four direct geometry spectrometers planned for spallation neutron source performance comparisons of four direct geometry spectrometers planned for spallation neutron source performance comparisons of four direct geometry spectrometers planned for spallation neutron source, Proceedings of ICANS-XVI (2003) 289.

[45] NumPy.
URL http://numpy.org

[46] S. Meyers, Effective C++: 55 Specific Ways to Improve Your Programs and Designs (3rd Edition), Addison-Wesley Professional, 2005.

[47] S. Meyers, More Effective C++: 35 New Ways to Improve Your Programs and Designs, Addison-Wesley Longman Publishing Co., Inc., Boston, MA, USA, 1995.

[48] J. Lakos, Large-scale C++ Software Design, Addison Wesley Longman Publishing Co., Inc., Redwood City, CA, USA, 1996.

[49] S. Ghali, Introduction to Geometric Computing, 1st Edition, Springer Publishing Company, Incorporated, 2008.

[50] P. K. Willendrup, E. Knudsen, K. Lefmann, E. Farhi, Component Manual for the Neutron Ray-Tracing Package McStas.
URL http://www.mcstas.org/documentation/manual/

[51] O. Arnold, J.-C. Bilheux, J. Borreguero, A. Buts, S. I. Campbell, L. Chapon, M. Doucet, N. Draper, R. F. Leal, M. Gigg, et al., Mantid-data analysis and visualization package for neutron scattering and $\mu$ sr experiments, Nuclear Instruments and Methods in Physics Research Section A: Accelerators, Spectrometers, Detectors and Associated Equipment 764 (2014) 156–166.

[52] J. Taylor, O. Arnold, J. Bilheaux, A. Buts, S. Campbell, M. Doucet, N. Draper, R. Fowler, M. Gigg, V. Lynch, et al., Mantid, a high performance framework for reduction and analysis of neutron scattering data, Bulletin of the American Physical Society 57.

[53] D. L. Abernathy, M. B. Stone, M. J. Loguillo, M. S. Lucas, O. Delaire, X. Tang, J. Y. Y. Lin, B. Fultz, Design and operation of the wide angular-range chopper spectrometer arcs at the spallation neutron source, Review of Scientific Instruments 83 (1) (2012) 015114–015114.

[54] G. E. Granroth, D. H. Vandergriff, S. E. Nagler, Sequoia: A fine resolution chopper spectrometer at the sns, Physica B: Condensed Matter 385-86 (Part 2) (2006) 1104–1106.

[55] G. E. Granroth, A. I. Kolesnikov, T. E. Sherline, J. P. Clancy, K. A. Ross, J. P. C. Ruff, B. D. Gaulin, S. E. Nagler, Sequoia: A newly operating chopper spectrometer at the sns, Journal of Physics: Conference Series 251 (1) (2010) 012058.

[56] B. Winn, U. Filges, V. Garlea, M. Graves-Brook, M. Hagen, C. Jiang, M. Kenzelmann, L. Passell, S. Shapiro, X. Tong, I. Zaliznyak, Recent progress on hyspec, and its polarization analysis capabilities, EPJ Web of Conferences.

[57] G. E. Granroth, M. Chen, J. A. Kohl, M. E. Hagen, J. W. Cobb, Fast monte carlo simulation of a dispersive sample on the sequoia spectrometer at the sns, Journal of Neutron Research 15 (1) (2007) 91–94.

[58] M. Hagen, B. Winn, V. Gosh, Private communication.

[59] M. Cohen, V. Heine, D. Weaire, The fitting of pseudopotentials to experimental data and their subsequent application, Solid State Phys. 24.

[60] G. Gilat, R. M. Nicklow, Normal vibrations in aluminum and derived thermodynamic properties, Phys. Rev. 143 (1966) 487–494. doi:10.1103/PhysRev.143.487.
URL http://link.aps.org/doi/10.1103/PhysRev.143.487

[61] M. Kresch, M. Lucas, O. Delaire, J. Y. Y. Lin, B. Fultz, Phonons in aluminum at high temperatures studied by inelastic neutron scattering, Phys. Rev. B 77 (2008) 024301. doi:10.1103/PhysRevB.77.024301.
URL http://link.aps.org/doi/10.1103/PhysRevB.77.024301

[62] X. Tang, C. W. Li, B. Fultz, Anharmonicity-induced phonon broadening in aluminum at high temperatures, Physical Review B 82 (18) (2010) 184301.

[63] M. D. Lumsden, S. E. Nagler, B. C. Sales, D. A. Tennant, D. F. McMorrow, S.-H. Lee, S. Park, Magnetic excitation spectrum of the square lattice S = 12 heisenberg antiferromagnet $k_2v_3o_8$, Phys. Rev. B 74 (2006) 214424. doi:10.1103/PhysRevB.74.214424.
URL http://link.aps.org/doi/10.1103/PhysRevB.74.214424

[64] P. J. Brown, Magnetic form factors, Vol. C of International Tables for Crystallography, D. Reidel Publishing, Dordrecht, Holland, 1983-1993, Ch. 4.4.5, pp. 391–399.

[65] G. Shirane, S. M. Shapiro, J. M. Tranquada, Neutron Scattering with a Triple-Axis Spectrometer, Cambridge University Press, 2002, cambridge Books Online.
URL http://dx.doi.org/10.1017/CBO9780511534881

[66] T. G. Perring, High energy magnetic excitations in hexagonal cobalt, dissertation, Cambridge University (1991).